

Synthesis of paracrystalline diamond

<https://doi.org/10.1038/s41586-021-04122-w>

Received: 18 April 2021

Accepted: 12 October 2021

Published online: 24 November 2021

 Check for updates

Hu Tang¹, Xiaohong Yuan¹, Yong Cheng², Hongzhan Fei³, Fuyang Liu¹, Tao Liang¹, Zhidan Zeng¹, Takayuki Ishii^{1,3}, Ming-Sheng Wang², Tomoo Katsura³, Howard Sheng⁴✉ & Huiyang Gou^{1,5}✉

合成方法 Solids in nature can be generally classified into crystalline and non-crystalline states^{1–7}, depending on whether long-range lattice periodicity is present in the material. The differentiation of the two states, however, could face fundamental challenges if the degree of long-range order in crystals is significantly reduced. Here we report a paracrystalline state of diamond that is distinct from either crystalline or amorphous diamond^{8–10}. The paracrystalline diamond reported in this work, consisting of sub-nanometre-sized paracrystallites that possess a well-defined crystalline medium-range order up to a few atomic shells^{4,5,11–13}, was synthesized in high-pressure high-temperature conditions (for example, 30 GPa and 1,600 K) employing face-centred cubic C₆₀ as a precursor. The structural characteristics of the paracrystalline diamond were identified through a combination of X-ray diffraction, high-resolution transmission microscopy and advanced molecular dynamics simulation. The formation of paracrystalline diamond is a result of densely distributed nucleation sites developed in compressed C₆₀ as well as pronounced second-nearest-neighbour short-range order in amorphous diamond due to strong sp³ bonding. The discovery of paracrystalline diamond adds an unusual diamond form to the enriched carbon family^{14–16}, which exhibits distinguishing physical properties and can be furthered exploited to develop new materials. Furthermore, this work reveals the missing link in the length scale between amorphous and crystalline states across the structural landscape, having profound implications for recognizing complex structures arising from amorphous materials.

结构表征和原因

意义

Amorphous solids refer to materials that do not possess long-range periodicity as exhibited in crystals^{1–11}. Consequently, Bragg peaks associated with crystalline arrangements of atoms are absent or obscured in the diffraction signals of amorphous materials, which renders the recognition of their structural organizations notoriously difficult. Owing to decades of research effort, it is now understood that structural ordering on the atomic level of amorphous solids is ubiquitous, as manifested by the short-range order (SRO) to medium-range order (MRO) in metallic glasses^{5–7} and the continuous random networks (CRNs) of amorphous semiconductors^{1–3}. Moving from the short range into the extended length scale abutting the long-range scale, however, our understanding of the structural arrangements remains much more limited, which is often complicated by capricious crystalline structural ordering encountered in amorphous materials^{13,17–19}. In an attempt to resolve this structural enigma, a paracrystalline structure model was proposed^{11,19}, in which nanosized paracrystallites were introduced to the amorphous matrix to account for the crystalline MRO. A crucial question to answer is, in the configurational space, whether we are able to identify a state of matter that is fully packed with tiny paracrystals possessing only MRO but devoid of long-range order (LRO). The identification of such a material state is essential to obtaining much-needed structural information differentiating amorphous solids

with and without crystalline MRO. This material state with dominating crystalline MRO would serve as the Rosetta stone to uncover the nature of a large set of non-crystalline materials. In this work, we report the discovery of such a substance in diamond, termed paracrystalline diamond (p-D).

Among myriads of carbon allotropes, diamond stands out as an important industrial material, featuring complete sp³ bonding. Diamond exists in many crystal forms, among which the most familiar are cubic diamond (CD) and hexagonal diamond (HD). However, unlike other four-fold-coordinated systems such as Si and Ge, synthesis of fully sp³-bonded amorphous carbon, or amorphous diamond (a-D), has proven difficult. Chemical vapour deposition and physical sputtering methods, approaches for forming amorphous Si or Ge, result only in diamond-like carbon (DLC) with variable sp³ fractions²⁰. Not until recently were Zeng et al. able to synthesize recoverable a-D by means of laser heating in a diamond-anvil cell (DAC)⁹. Structure-wise, the as-obtained a-D can be described by the CRN model, in line with other tetrahedral amorphous systems. It was also reported that a-D can be produced by shock compression involving highly nonequilibrium high-pressure and high-temperature (HP-HT) conditions⁸.

The current realization of a-D requires relatively high pressure (40–55 GPa) and a rapid cooling rate (10⁶–10¹⁰ K s^{−1})^{8,9}, and the finite sample

¹Center for High Pressure Science and Technology Advanced Research, Beijing, China. ²State Key Laboratory of Physical Chemistry of Solid Surfaces, College of Materials, Xiamen University, Xiamen, China. ³Bayerisches Geoinstitut, University of Bayreuth, Bayreuth, Germany. ⁴Department of Physics and Astronomy, George Mason University, Fairfax, VA, USA. ⁵College of Environmental and Chemical Engineering, Yanshan University, Qinhuangdao, China. ✉e-mail: hsheng@gmu.edu; huiyang.gou@hpstar.ac.cn

size (several tens of micrometres) inevitably hampers our understanding of the structure, properties and synthesis mechanism. As such, synthesizing large and high-quality a-D remains both highly demanding and technically challenging. In this study, we attempted to synthesize millimetre-sized non-crystalline diamond using a large-volume multi-anvil press (MAP). Conventional MAP technology could not generate such ultrahigh pressures in a millimetre-sized sample. However, our recently developed ultrahigh-pressure technique using MAP is capable of generating pressures to 50 GPa in millimetre-sized samples²¹. Using this technique, we succeeded in synthesizing p-D with a 1.0 mm diameter at a pressure of 30 GPa. We present details regarding the synthesis and structural analyses of this sample and articulate the synthesis mechanism below.

We selected zero-dimensional fullerene (C_{60}) in a face-centred cubic (fcc) crystal to monitor its phase evolution at 30 GPa and a temperature range of 1,200–1,800 K. Previous investigations have demonstrated that C_{60} can transform into polymerized C_{60} crystals and disordered sp^2 – sp^3 carbon under HP–HT (13–25 GPa)^{22–26}. Here, at an elevated pressure condition of 30 GPa, the X-ray diffraction (XRD) patterns of the recovered samples synthesized at various temperatures are shown in Fig. 1a and Extended Data Fig. 1a. The diffraction signals are distinctly different from the initial fcc C_{60} (Fig. 1b), signalling the formation of new phases. Broadened diffraction peaks around ~2.9, ~5.4 and ~8.4 Å⁻¹ are reminiscent of amorphous materials, bearing considerable resemblance to those of a-D (ref. ⁹) and DLC carbon with a high fraction of sp^3 bonds²⁴. Moreover, the recovered samples heated above 1,400 K are highly transparent (for example, Fig. 1a inset), suggesting a dense diamond-like (sp^3 -dominated) structure. To quantitatively examine the composition of sp^2 versus sp^3 in the samples, we utilized Raman and electron energy loss spectroscopy (EELS)^{27,28}. Raman and EELS characterizations (Fig. 1c, d and Extended Data Fig. 1) indicate that the sample recovered from 1,400 K contains a residual amount (~5.2%) of sp^2 bonds, whereas samples from above 1,400 K are completely sp^3 -bonded, demonstrating successful synthesis of non-crystalline diamond at a pressure much lower than previously reported^{8,9}. The densities of the samples at 1,500 and 1,600 K are estimated to be 3.20 and 3.25 g cm⁻³ (Extended Data Fig. 1), respectively, close to that of a-D (3.30 g cm⁻³)^{8,9}. Further increasing the temperature to 1,800 K leads to temperature-induced crystallization (Extended Data Fig. 1a).

High-resolution transmission electron microscopy (HRTEM) images of the recovered samples are shown in Fig. 2 and Extended Data Fig. 2. Lattice fringes associated with LRO are not found in the HRTEM images, indicating the disordered nature of the samples beyond a certain length (~1 nm). We randomly selected small regions (7.0×7.0 nm²) and conducted fast Fourier transformation (FFT) to obtain the scattering signals in the momentum space. The diffuse haloes of the FFT patterns corresponding to the selected areas confirm the overall amorphous feature, consistent with the XRD results. On a finer scale, however, visual inspections indicate that the images become more ordered for samples synthesized at elevated temperatures, which is also evidenced by the narrowing FFT rings with increasing temperature. The ordered HRTEM images resemble those of amorphous Si films and bulk metallic glasses with MRO structures^{17,29,30}, but they differ from the previously reported a-D described with the CRN model⁹. For the samples annealed at 1,400–1,600 K, a considerable amount of ordered clusters within 0.5–1.0 nm are visible in the HRTEM images. Within the spatial distance of ~1.0 nm, two types of lattice fringes are identifiable, which are found to be close to the atomic arrangements along the [110] and [010] zone axes of CD and HD, respectively, as shown in Fig. 2f. This finding is further validated by the FFT patterns of the selection areas (2.0×2.0 nm²), where the intensified ‘diffraction’ spots matching CD or HD crystalline order are recognizable. Note that both cubic and hexagonal MRO clusters are highly distorted because the inclusive angles ($72.1 \pm 1.5^\circ$ for cubic and $89.5 \pm 2.5^\circ$ for hexagonal) of the lattice fringes deviate from those of pristine CD (70.3°) and HD (90°) crystals³¹. The observed

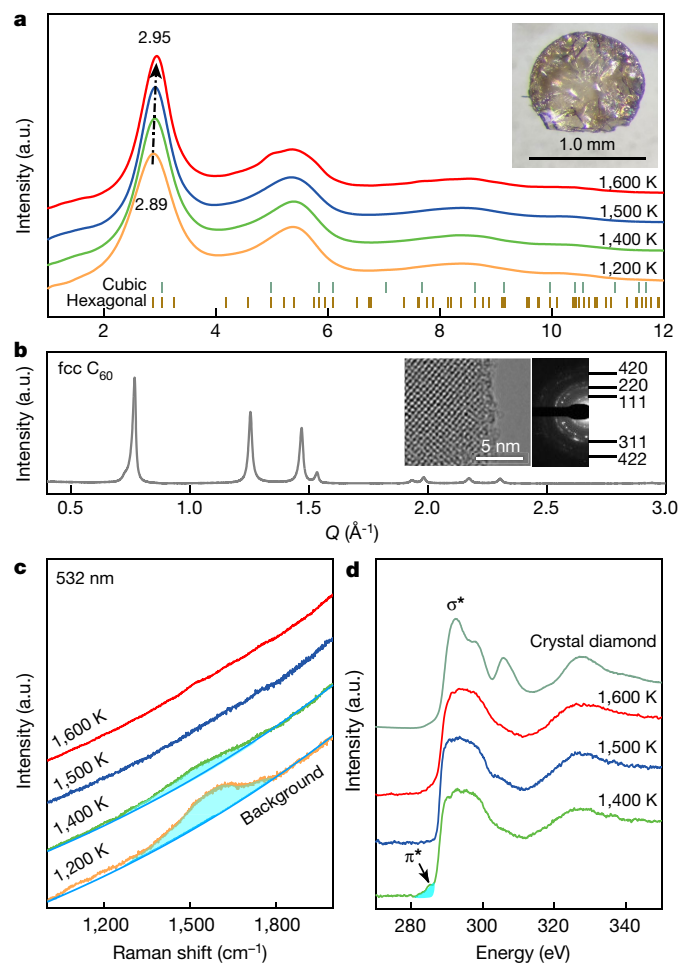


Fig. 1 | Synthesizing fully sp^3 -bonded carbon samples at 30 GPa and 1,200–1,600 K for 10 min. **a**, XRD patterns indicate direct synthesis of disordered carbon from C_{60} under 30 GPa. With increasing temperature, the first main diffraction peak shifts from 2.89 to 2.95 Å⁻¹, suggesting an increased density at higher temperatures. Inset: a typical optical photograph of the transparent bulk sample (~1 mm in diameter) obtained at 30 GPa and 1,600 K. **b**, XRD pattern of the C_{60} precursor ($Fm\bar{3}m$). Inset: corresponding HRTEM image and selected-area electron diffraction pattern. **c**, Visible Raman (wavelength of 532 nm) spectra of samples recovered from different temperatures. The samples annealed at 1,200 K and 1,400 K have similar Raman features with the DLC films having a high sp^3 fraction²⁷, suggesting a trace amount of sp^2 carbon remaining in these samples. **d**, EELS spectra of samples recovered from different temperatures and CD crystal. The features at 285 and 292 eV are due to transitions of a 1s electron to π^* and σ^* , corresponding to sp^2 and sp^3 bonding, respectively. The 1,400 K sample has a residual 5.2% of sp^2 bonds, analysed from the ratio of π^* and σ^* features using single-crystal graphite for calibration²⁸.

morphology of the as-synthesized non-crystalline diamond is clearly distinguished from a-D, hinting at the formation of crystalline MRO structures dominating the samples.

To uncover the hidden structural ordering in the obtained non-crystalline diamond, we relied on large-scale classical molecular dynamics (MD) simulation³² employing a recently developed realistic angular-dependent potential for carbon³³ and adiabatic-bias MD³⁴ to accelerate dynamics. Starting from fcc C_{60} and mimicking the experimental HP–HT conditions (for example, 1,600 K and 30 GPa), we revealed how the fullerene evolves into the non-crystalline diamond deterministically. On the formation of nearly complete sp^3 bonding at 1,600 K, small but prolific clusters with CD- and HD-like atomic packing gradually take form. These MRO clusters typically encompass

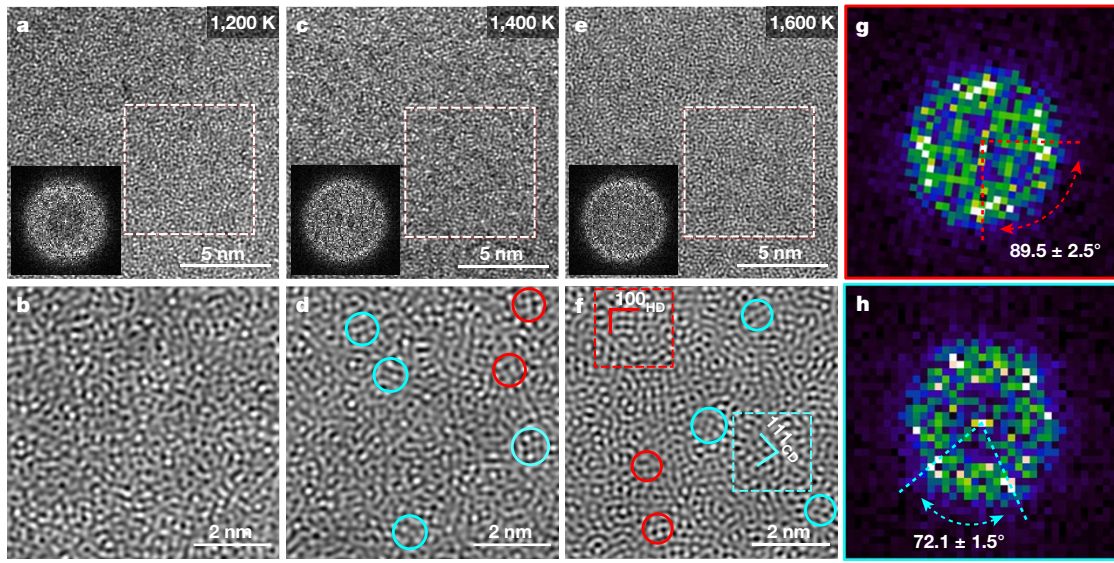


Fig. 2 | HRTEM characterization of samples recovered from 30 GPa and 1,200–1,600 K. a–f, Typical HRTEM images of samples and the corresponding inverse FFT images, respectively. Insets: FFT patterns corresponding to the white boxes ($7.0 \times 7.0 \text{ nm}^2$) in a, c and e, respectively. The cyan and red circles in d and f indicate crystal-like MRO clusters. Note that the circles serve only as a guide for the eye. MRO clusters are discernable in f, where the lattice fringes

marked by the cyan and red solid lines match CD- and HD-like (111) and (100) crystal planes, respectively. g, h, FFT patterns, corresponding to the red and cyan boxes ($2.0 \times 2.0 \text{ nm}^2$) in f, respectively. The brighter spots on the diffuse haloes indicated by the coloured arrows confirm the existence of CD- and HD-like MRO clusters illustrated in f.

4–5 atomic shells, henceforth referred to as paracrystallites. With prolonged simulation time, the amount of paracrystallites increases and eventually saturates at a volume fraction of $\phi = 0.7$, which is rationalized to be the maximum paracrystal content attainable in the given simulation condition due to thermodynamic constraints. Above a certain threshold (for example, $\phi = 0.3$), the paracrystallites start to interconnect and percolate, which is a distinguishing feature of the material.

Structural differences of non-crystalline materials are identified by the structure factor $S(Q)$. Subtle but definite differences in $S(Q)$ (for example, a-D versus p-D) can be experimentally discriminated for closely related structures. In our simulation, we accurately determined $S(Q)$ from the atomistic models based on the Ornstein-Zernike equation³⁵ (see Methods). The comparison of the simulated $S(Q)$ of a-D and p-D ($\phi = 0.7$) is provided in Fig. 3a. While both $S(Q)$ profiles are characteristic of non-crystalline materials, the differences are conspicuous, evidenced by peak intensity variations. For a-D, the intensity of the first main diffraction peak at $\sim 2.9 \text{ \AA}^{-1}$ is lower than that of the second peak at $\sim 5.4 \text{ \AA}^{-1}$. In comparison to a-D, as the volume fraction of paracrystallites increases, the intensity of the first peak monotonically rises, accompanied by a decrease in the intensity of the second peak (Extended Data Fig. 3a). The intensity ratio of the first peak to the second peak I_1/I_2 is positively correlated to the degree of MRO arrested in the sample. This relationship is thus used to estimate the content of paracrystallites in the experimental samples. Indeed, the extracted $S(Q)$ of the synthesized samples from the XRD patterns³⁶ in Fig. 1 exhibits exactly the same predictive trend (Fig. 3b). Plotting I_1/I_2 against the paracrystal volume fraction ϕ , we find that high proportions of paracrystallites exist in the samples above 1,400 K (Fig. 3c). For instance, the amount of paracrystallites reaches as high as 47% and 52% for samples at 1,500 and 1,600 K, similar to those (46% and 48%) obtained from HRTEM images using autocorrelation function analysis¹⁷. A satisfactory match between the $S(Q)$ of a paracrystalline model ($\phi = 0.5$) and that of the 1,500 K sample is achieved. Figure 3d presents the structural model of a homogeneous p-D with 70% CD- and HD-like paracrystallites (~0.8–1.0 nm in size) and the remaining 30% a-D. The simulated HRTEM image of this atomistic model (Fig. 3e) is in striking agreement with the experimental ones, validating the paracrystalline nature of the samples at 1,500 and 1,600 K.

To further distinguish the structural difference between a-D and p-D and enable identification of CD- or HD-like atomic packing in p-D, we employed the common-neighbour analysis (CNA)³⁷ and orientational order analysis methods³⁸. Figure 4a illustrates the atomic structures of p-D and a-D visualized on the basis of their respective degree of MRO. Through CNA, high fractions of CD- and HD-like clusters are found to be abundant in p-D, but they are starkly absent in a-D. Moreover, the corresponding atomic structure of p-D visualized by the orientational order parameter \bar{q}_6 (ref. ³⁸) reveals the orientational order of the local clusters, supporting the presence of MRO clusters in p-D. To shed light on the size of the paracrystallites, we adopted an orientational correlation function $\kappa(r)$ (defined in the Methods). Figure 4b shows the radial distribution functions $g(r)$ and the orientational correlation functions of p-D and a-D, respectively. Both a-D and p-D have nearly the same $g(r)$ profile for the first peak, in agreement with their respective tetrahedral atomic environments. However, the intensity of the first peak in the $\kappa(r)$ of a-D is significantly lower than that of p-D where just two peaks are visible in the profile, suggesting that a-D has SRO within two coordination shells. In contrast, the first five sharp peaks in p-D indicate the strong MRO, and the subsequent three peaks are weakened and broadened because of the absence of LRO. Previously, nano-polycrystalline diamond (NPD) with ultrafine grains has been synthesized from various sp^2 carbons including C_{60} under HP-HT conditions^{39–43}. Our simulations of NPD with different grain sizes (1.20–2.40 nm) reveal a completely different morphology in NPD due to the presence of LRO (Extended Data Fig. 3). The paracrystallites in p-D are found to be severely distorted in comparison to perfect diamond lattices of which the level of distortion is on par with the grain-boundary atoms of ultrafine NPD (Extended Data Figs. 3c and 4d). This accounts for the absence of Bragg diffraction peaks from its XRD pattern.

We attribute the formation of p-D to two main factors (see Methods). First, we discovered that the CRN-type a-D exhibits strong diamond-like SRO in the first two atomic shells (16 atoms), in comparison to that of amorphous Si (Extended Data Figs. 4 and 5). This is consistent with the argument that sp^3 carbon has the largest tetrahedral parameter among all group IV elements⁴⁴. The pronounced intrinsic diamond-like SRO of a-D greatly facilitates the development of MRO, and consequently

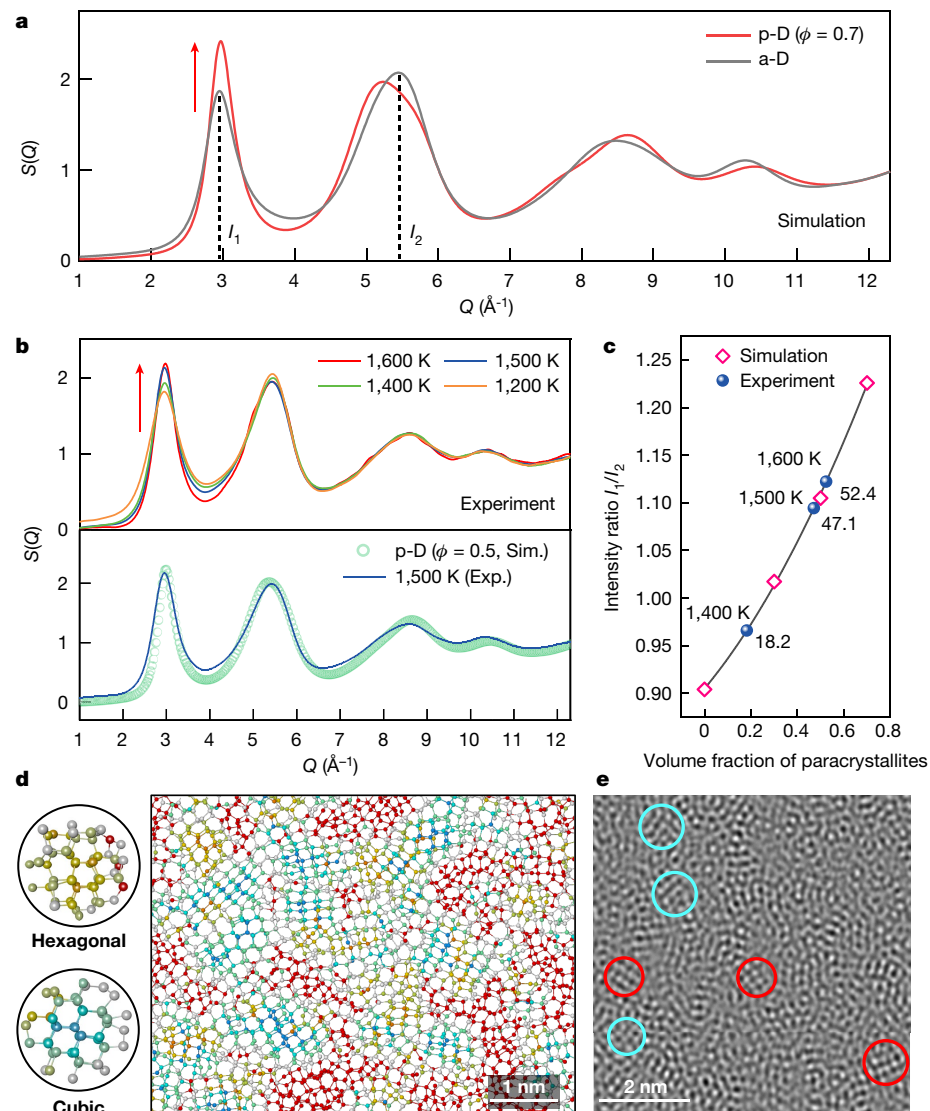


Fig. 3 | Identification of p-D. **a**, Simulated structure factor $S(Q)$ of a-D and p-D ($\phi = 70\%$). **b**, Top: experimental $S(Q)$ of the recovered samples. Bottom: simulated $S(Q)$ of p-D with 50% paracrystallites in comparison to the experimental data. **c**, Intensity ratio of the first peak ($\sim 2.9 \text{ \AA}^{-1}$) to the second peak ($\sim 5.4 \text{ \AA}^{-1}$) as a function of volume percentage of paracrystallites. **d**, Structural model of p-D with 70% paracrystallites from **MD simulation**. Colours represent different types of atomic packing. On the basis of CNA, the

turquoise, gold and red atoms represent CD-like, HD-like and disordered atomic packing within two atomic shells, respectively. The typical size and atomic arrangement of the paracrystallites are illustrated in the circles on the left. The volume ratio between CD and HD paracrystallites is roughly 1.5:1. **e**, Simulated HRTEM image from the paracrystalline model presented in **d**. The cyan and yellow circles indicate CD- and HD-like clusters, respectively, in agreement with the experimental HRTEM image shown in Fig. 2f.

the formation of diamond paracrystallites. Second, the successful synthesis of p-D depends highly on the structure of the C_{60} precursor. We argue that the formation of p-D is a result of a nucleation-controlled process, where the formation of orientationally correlated sp^3 bonds between neighbouring C_{60} units offers fertile sites for nucleation. Our simulated results (see Methods and Extended Data Figs. 6–10 for details) demonstrate that the formation of p-D goes through three main stages: inter-buckyball bond connection (15% sp^3 bonds) during compression to 30 GPa at room temperature; kinetically controlled polymerization and collapse of buckyballs during heating to 1,600 K at 30 GPa; and the formation of p-D from a-D during isothermal annealing at 1,600 K and 30 GPa. In particular, the sp^3 bonds formed in the early stage of polymerization are orientationally ordered in the local contact regions (Extended Data Fig. 6), which persists into the a-D state at high temperatures and contributes to the formation of p-D. Abundant and homogeneous sp^3 bonding of C_{60} by polymerization under high pressure and low temperature prevents the otherwise heterogeneous

nucleation and growth of crystals, allowing the formation of p-D in a divide-and-conquer manner. To further understand the critical role of C_{60} in the formation of p-D, we examined other sp^2 -dominated carbons in experiments (carbon onion and type-1 glassy carbon) as a precursor in the same HP-HT conditions, which failed to synthesize p-D in our experiments (Extended Data Fig. 1a). Additionally, we surmise that the bundled single-walled carbon nanotubes with well-aligned carbon bonds may provide abundant sp^3 bonding sites through intermolecular polymerization under high pressure⁴⁵, like in C_{60} , allowing for the synthesis of p-D.

The unique MRO structures of p-D elicit new physical properties. The mechanical properties of p-D were assessed by the measurements of Vickers and nanoindentation hardness. p-D exhibits highly isotropic Vickers hardness H_V of 116.1 ± 3.6 GPa and nanoindentation hardness H_N of 102.1 ± 1.4 GPa (Extended Data Fig. 11), comparable with natural diamond⁴². The obtained Young's modulus E (937.2 ± 10.1 GPa), shear modulus G (437.9 ± 4.7 GPa) and bulk modulus K (363.3 ± 3.9 GPa)

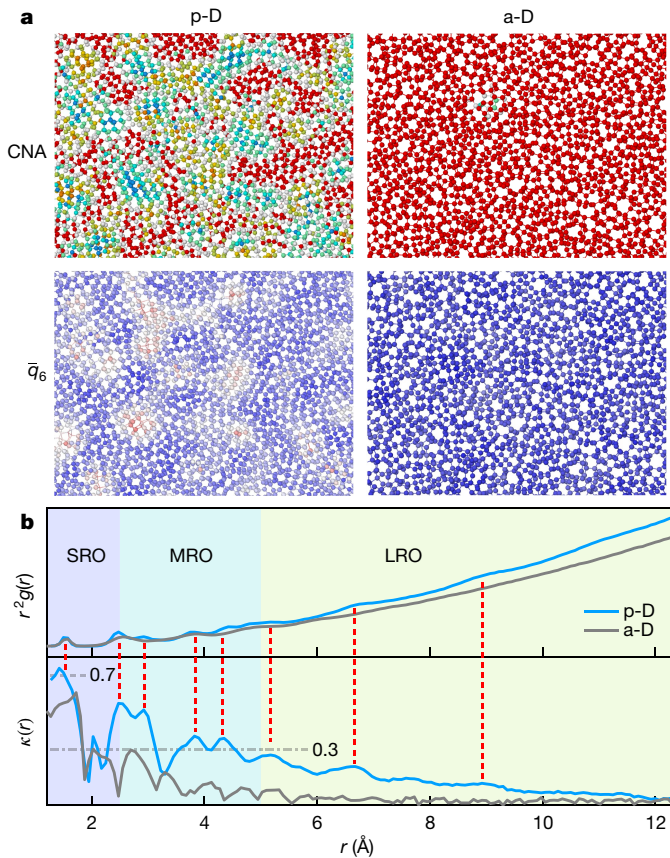


Fig. 4 | Distinguishing p-D from a-D. **a**, Atomic structure of p-D versus a-D, visualized on the basis of their respective degree of MRO represented by the CNA index and orientational order parameter \bar{q}_6 . For a-D, the images present monotonous colours (red and blue), indicating the absence of crystal-like MRO clusters. In contrast, high-MRO-fraction CD- and HD-like clusters populate and become the main feature in p-D. **b**, The radial distribution function $g(r)$ (top) and orientational correlation function $k(r)$ (bottom) of p-D and a-D.

of p-D are close to those of diamond (1140 GPa, 535 GPa and 443 GPa)⁴⁶, consistent with our ab initio predictions (Extended Data Fig. 11e), making it an appealing candidate for ultrahard materials. Moreover, a measurement of thermostability of p-D in the air (Extended Data Fig. 12) gives an onset oxidation temperature of 950 K, much higher than those (673–873 K) of DLC films⁴⁷, nano diamond⁴⁸, chemical-vapour-deposited diamond⁴⁹ and NPD. These outstanding combinations of mechanical properties and oxidation resistance endow p-D with great potential for niche technological applications. Last, we point out that the paracrystalline state diamond may exist in other forms (for example, with different types and compositions of paracrystallites contingent on the starting material and synthesis conditions), waiting to be explored to obtain novel carbon materials with unusual properties.

Online content

Any methods, additional references, Nature Research reporting summaries, source data, extended data, supplementary information, acknowledgements, peer review information; details of author contributions and competing interests; and statements of data and code availability are available at <https://doi.org/10.1038/s41586-021-04122-w>.

1. Zallen, R. *The Physics of Amorphous Solids* (Wiley, 1983).
2. Zachariassen, W. H. The atomic arrangement in glass. *J. Am. Chem. Soc.* **54**, 3841–3851 (1932).
3. Elliott, S. R. A continuous random network approach to the structure of vitreous boron trioxide. *Philos. Mag. B* **37**, 435–446 (1978).
4. Elliott, S. R. Medium-range structural order in covalent amorphous solids. *Nature* **354**, 445–452 (1991).
5. Sheng, H. W., Luo, W. K., Alamgir, F. M., Bai, J. M. & Ma, E. Atomic packing and short-to-medium-range order in metallic glasses. *Nature* **439**, 419–425 (2006).
6. Miracle, D. B. A structural model for metallic glasses. *Nat. Mater.* **3**, 697–702 (2004).
7. Hirata, A. et al. Direct observation of local atomic order in a metallic glass. *Nat. Mater.* **10**, 28–33 (2011).
8. Hirai, H., Kondo, K., Yoshizawa, N. & Shiraishi, M. Amorphous diamond from C_{60} fullerene. *Appl. Phys. Lett.* **64**, 1797–1799 (1994).
9. Zeng, Z. et al. Synthesis of quenchable amorphous diamond. *Nat. Commun.* **8**, 322 (2017).
10. Lin, Y. et al. Amorphous diamond: a high-pressure superhard carbon allotrope. *Phys. Rev. Lett.* **107**, 175504 (2011).
11. Treacy, M. M. J. & Borisenko, K. B. The local structure of amorphous silicon. *Science* **335**, 950–953 (2012).
12. Leocmach, M. & Tanaka, H. Roles of icosahedral and crystal-like order in the hard spheres glass transition. *Nat. Commun.* **3** (2012).
13. Gibson, J. M., Treacy, M. M. J., Sun, T. & Zaluzec, N. J. Substantial crystalline topology in amorphous silicon. *Phys. Rev. Lett.* **105** (2010).
14. Oganov, A. R., Hemley, R. J., Hazen, R. M. & Jones, A. P. Structure, bonding, and mineralogy of carbon at extreme conditions. *Rev. Mineral. Geochem.* **75**, 47–77 (2013).
15. Georgakilas, V., Perman, J. A., Tucek, J. & Zboril, R. Broad family of carbon nanoallotropes: classification, chemistry, and applications of fullerenes, carbon dots, nanotubes, graphene, nanodiamonds, and combined superstructures. *Chem. Rev.* **115**, 4744–4822 (2015).
16. Németh, P. et al. Complex nanostructures in diamond. *Nat. Mater.* **19**, 1126–1131 (2020).
17. Sarac, B. et al. Origin of large plasticity and multiscale effects in iron-based metallic glasses. *Nat. Commun.* **9** (2018).
18. Hwang, J. et al. Nanoscale structure and structural relaxation in $Zr_{50}Cu_{45}Al_5$ bulk metallic glass. *Phys. Rev. Lett.* **108** (2012).
19. Voyles, P. M. et al. Structure and physical properties of paracrystalline atomistic models of amorphous silicon. *J. Appl. Phys.* **90**, 4437–4451 (2001).
20. Robertson, J. Diamond-like amorphous carbon. *Mater. Sci. Eng. R Rep.* **37**, 129–281 (2002).
21. Ishii, T., Liu, Z. & Katsura, T. A breakthrough in pressure generation by a Kawai-type multi-anvil apparatus with tungsten carbide anvils. *Engineering* **5**, 434–440 (2019).
22. Iwasa, Y. et al. New phases of C_{60} synthesized at high pressure. *Science* **264**, 1570–1572 (1994).
23. Blank, V. D. et al. Phase transformations in solid C_{60} at high-pressure-high-temperature treatment and the structure of 3D polymerized fullerenes. *Phys. Lett. A* **220**, 149–157 (1996).
24. Zhang, S. et al. Discovery of carbon-based strongest and hardest amorphous material. Preprint at <https://arxiv.org/abs/2011.14819> (2020).
25. Yamanaka, S. et al. Electron conductive three-dimensional polymer of cuboidal C_{60} . *Phys. Rev. Lett.* **96**, 076602 (2006).
26. Sundqvist, B. Carbon under pressure. *Phys. Rep.* **909**, 1–73 (2021).
27. Ferrari, A. C. & Robertson, J. Raman spectroscopy of amorphous, nanostructured, diamond-like carbon, and nanodiamond. *Philos. Trans. R. Soc. Lond. A Math. Phys. Eng. Sci.* **362**, 2477–2512 (2004).
28. Daniels, H., Brydson, R., Rand, B. & Brown, A. Investigating carbonization and graphitization using electron energy loss spectroscopy (EELS) in the transmission electron microscope (TEM). *Philos. Mag. B* **87**, 4073–4092 (2007).
29. Chen, L. J. et al. Structural evolution in amorphous silicon and germanium thin films. *Microsc. Microanal.* **8**, 268–273 (2002).
30. Wang, Q. et al. The atomic-scale mechanism for the enhanced glass-forming-ability of a Cu-Zr based bulk metallic glass with minor element additions. *Sci. Rep.* **4** (2014).
31. Tang, H. et al. Revealing the formation mechanism of ultrahard nanotwinned diamond from onion carbon. *Carbon* **129**, 159–167 (2018).
32. Plimpton, S. Fast parallel algorithms for short-range molecular dynamics. *J. Comput. Phys.* **117**, 1–19 (1995).
33. Zhu, S.-c., Yan, X.-z., Liu, J., Oganov, A. R. & Zhu, Q. A revisited mechanism of the graphite-to-diamond transition at high temperature. *Matter* **3**, 864–878 (2020).
34. Marchi, M. & Ballone, P. Adiabatic bias molecular dynamics: a method to navigate the conformational space of complex molecular systems. *J. Chem. Phys.* **110**, 3697–3702 (1999).
35. Lee, L. L. *Molecular Thermodynamics of Electrolyte Solutions* (World Scientific, 2008).
36. Sheng, H. W. et al. Polyamorphism in a metallic glass. *Nat. Mater.* **6**, 192–197 (2007).
37. Faken, D. & Jónsson, H. Systematic analysis of local atomic structure combined with 3D computer graphics. *Comput. Mater. Sci.* **2**, 279–286 (1994).
38. Lechner, W. & Dellago, C. Accurate determination of crystal structures based on averaged local bond order parameters. *J. Chem. Phys.* **129**, 114707 (2008).
39. Irifuné, T., Kurio, A., Sakamoto, S., Inoue, T. & Sumiya, H. Ultrahard polycrystalline diamond from graphite. *Nature* **421**, 599–600 (2003).
40. Dubrovinskaia, N., Dubrovinsky, L., Langenhorst, F., Jacobsen, S. & Liebske, C. Nanocrystalline diamond synthesized from C_{60} . *Diam. Relat. Mater.* **14**, 16–22 (2005).
41. Sumiya, H. & Irifuné, T. Hardness and deformation microstructures of nano-polycrystalline diamonds synthesized from various carbons under high pressure and high temperature. *J. Mater. Res.* **22**, 2345–2351 (2007).
42. Huang, Q. et al. Nanotwinned diamond with unprecedented hardness and stability. *Nature* **510**, 250–253 (2014).
43. Tang, H. et al. Synthesis of nano-polycrystalline diamond in proximity to industrial conditions. *Carbon* **108**, 1–6 (2016).

Article

44. Hujo, W., Shadrack Jubes, B., Rana, V. K., Chakravarty, C. & Molinero, V. The rise and fall of anomalies in tetrahedral liquids. *J. Stat. Phys.* **145**, 293–312 (2011).
45. Merlen, A. et al. High pressure–high temperature synthesis of diamond from single-wall pristine and iodine doped carbon nanotube bundles. *Carbon* **47**, 1643–1651 (2009).
46. Teter, D. M. Computational alchemy: the search for new superhard materials. *MRS Bull.* **23**, 22–27 (1998).
47. Bewilogua, K. & Hofmann, D. History of diamond-like carbon films — from first experiments to worldwide applications. *Surf. Coat. Technol.* **242**, 214–225 (2014).
48. Osswald, S., Yushin, G., Mochalin, V., Kucheyev, S. O. & Gogotsi, Y. Control of sp^2/sp^3 carbon ratio and surface chemistry of nanodiamond powders by selective oxidation in air. *J. Am. Chem. Soc.* **128**, 11635–11642 (2006).
49. Pu, J.-C., Wang, S.-F. & Sung, J. C. High-temperature oxidation behaviors of CVD diamond films. *Appl. Surf. Sci.* **256**, 668–673 (2009).

Publisher's note Springer Nature remains neutral with regard to jurisdictional claims in published maps and institutional affiliations.

© The Author(s), under exclusive licence to Springer Nature Limited 2021

Methods

Sample synthesis

The starting material, C₆₀, was purchased from Alfa Aesar. HP-HT experiments were performed using an ultrahigh-pressure MAP⁵⁰ at the Bayerisches Geoinstitut of the University of Bayreuth in Germany and the Center for High Pressure Science & Technology Advanced Research (HPSTAR) in China. The synthetic pressure was set to 30 GPa, implemented using carbide anvils with 3-mm truncation and 7-mm MgO + 5 wt% Cr₂O₃ octahedron. The temperature range was from 1,200 to 1,800 K, generated using a LaCrO₃ heater. The pressure was calibrated at 2,300 K by evaluating the Al₂O₃ content in bridgmanite⁵¹, and the temperature was monitored using a type-D thermocouple. The starting material was pre-compressed into Pt capsules with diameters of 0.8 and 1.2 mm and a height of 1.6 mm at a pressure of 200 MPa. The samples were compressed to 30 GPa in 7 h at room temperature and heated to the designated temperatures with a heating rate of 100 K s⁻¹. In situ Raman spectroscopy (532 nm) of C₆₀ under high pressure was conducted without pressure-transmitting medium by using a symmetrical DAC with a culet size of 300 μm. The samples and ruby spheres for pressure calibration were loaded into the DAC sample chamber of 120 μm in diameter with a pre-indented rhenium gasket.

Structure characterization

To collect high-quality XRD data, the powder mode of a Bruker D8 Venture diffractometer equipped with Mo Kα radiation was employed. The samples were fixed on an organic XRD holder and rotated 720° in total within an acquisition time of 10 min. A background file was obtained with an empty organic holder with the same collection condition. To extract the structure factors from the XRD data, we followed the optimization method proposed in ref.³⁶. The microscopic structures of the samples were characterized by the FEI Talos-F200s transmission electron microscope operated with an accelerating voltage of 200 keV. The bonding analysis of the samples was performed by using Raman spectroscopy and EELS. The Raman spectra were acquired with two different wavelengths (325 nm and 532 nm) of laser excitation by using a Renishaw-type micro-Raman spectroscopy system. The EELS data were obtained using the ARM-200F (JEOL) microscope equipped with a spherical aberration corrector (CEOS).

Property measurements

The Vickers hardness H_v and fracture toughness K_{IC} were measured using a micro-Vickers hardness tester (Q10A⁺, Qness) with a Vickers diamond indenter at 4.9 and 9.8 N for a holding time of 15 s. H_v and K_{IC} were determined from the following equations⁴²:

$$H_v = \frac{1854.4F}{L^2} \quad (1)$$

$$K_{IC} = \frac{0.016(E/H_v)^{0.5}F}{C^{1.5}} \quad (2)$$

where F (N) is the applied load, L (μm) is the arithmetic mean of the two diagonals of the Vickers indentation, C (μm) is the average length of the radial cracks and E is Young's modulus of p-D.

The nanoindentation hardness (H_N) was measured with a three-sided pyramidal Berkovich diamond indenter (Keysight Nano Indenter G200), and the samples were loaded to the maximum load of 50 mN at a loading rate of 2 mN s⁻¹ with a holding time of 10 s. The Young's modulus (E) was derived from the loading/unloading-displacement curves according to the Oliver-Pharr method⁵². The values of Vickers hardness, nanoindentation hardness and Young's modulus (E) are given as an average value taken from more than five tests. The nanoindentation data of p-D were calibrated with natural diamond (100) surface.

The thermostability was evaluated using a thermogravimeter and differential scanning calorimeter, NETZSCHSTA 449 C, from room temperature to 1,773 K in the air with a heating rate of 5 K min⁻¹.

Computational methods

Structural model of a-D. In this work, a-D was obtained by conducting extensive ab initio MD simulations, following the protocol introduced in our previous work⁹. To yield better statistics, our simulation system was enlarged to 500 carbon atoms. Ab initio MD was performed with the density-functional-theory-based Vienna Ab-initio Simulation Package⁵³. The projector-augmented wave potential⁵⁴ with a valence configuration of 2s2p and the generalized gradient approximation were used in the simulation. The kinetic energy cutoff was set to 400 eV, and the simulation was conducted on the gamma point only. In brief, liquid carbon was slowly quenched from 5,000 to 300 K in an NPT (constant number of atoms, pressure and temperature) ensemble under a hydrostatic pressure condition of 50 GPa. The cooling rate was 2.5 × 10¹³ K s⁻¹. A phase transition during the quench process leads to the formation of a-D. The as-obtained high-pressure a-D structure was gradually relaxed to ambient pressure using a conjugate-gradient geometric optimization method. To cross-check the structure resulting from ab initio modelling, a different route was employed to generate a-D. In this approach, we applied the bond-switching algorithm⁵⁵, also known as the WWW method, to generate ideal CRN configurations with different sizes employing the Keating interatomic potential⁵⁶. The 500-atom CRN structure was further subjected to simulated annealing via ab initio MD to minimize local stresses and to achieve a more realistic structural model.

Structural model of p-D and phase transition from C₆₀ to p-D under HP-HT. Both classical MD³² and ab initio MD simulations were carried out to study the structure evolution of C₆₀ under HP-HT conditions and simulate the formation of p-D. For classical MD, a newly developed angular-dependent interatomic potential (C-ADP)^{33,57} was used to describe carbon. The development of the realistic C-ADP potential was based on mapping the complex energy landscape obtained with density-functional-theory-based calculations of more than 5,000 atomic configurations of C (>10⁶ atoms in the fitting database)^{58,59}. The empirical potential has been tested to be reliable in describing carbon phase behaviours over a wide temperature and pressure range (0–100 GPa) without compromising the computational speed, enabling us to simulate large samples across an extended temporal scale (in the sub-microsecond regime). The detailed MD simulation steps are as follows.

- 1) A 36,000-atom fcc-C₆₀ crystal was created with C₆₀ buckyballs randomly oriented. The fcc-C₆₀ crystal was equilibrated at 300 K and zero pressure for 1 ns.
- 2) The well-equilibrated C₆₀ crystal was compressed to 30 GPa at room temperature at a constant compression rate of 0.5 GPa ns⁻¹.
- 3) The system was brought up to 1,600 K at 30 GPa at a constant heating rate of 1.0 × 10⁶ K s⁻¹.
- 4) The system was subjected to long-time annealing at 1,600 K and 30 GPa, up to 15 ns.
- 5) The brute-force MD faces great challenges in extending the timescale to minutes (necessary for the formation of p-D). To circumvent this discrepancy, enhanced sampling approaches must be taken. Here, to bridge the temporal gap between experiment and simulation, we enabled an adiabatic-bias MD (ABMD) technique³⁴ to accelerate the dynamics, which was tested to be a more effective approach than other barrier-crossing techniques such as metadynamics⁶⁰ and the extended Lagrangian method⁶¹.

In the ABMD simulations stated above, a biasing potential was added to act on a collective variable, driving the system away from the amorphous state and gearing towards the formation of paracrystallites. In this work, the mean value of the order parameter \bar{q}_6^a (that is, $\bar{q}_6^a = \sum_i^N \bar{q}_6^i / N$, where N refers to the total number of atoms) was used as a collective

Article

variable. The parameter \bar{q}_6 for a particular atom is a coarse-grained quantity that measures the extent to which the orientation of the atoms in the coordination shells matches the orientation of the central atom, revealing the crystalline MRO. The definition of \bar{q}_6^i is given in the following section. The biasing potential V in the ABMD simulation was constructed as:

$$V[\emptyset(t)] = \begin{cases} \frac{1}{2}K[\emptyset(t) - \emptyset_m(t)]^2 & \text{for } \emptyset(t) > \emptyset_m(t) \\ 0 & \text{for } \emptyset(t) \leq \emptyset_m(t) \end{cases} \quad (3)$$

where $\emptyset(t) = [\bar{q}_6^a(t) - \bar{q}_6^t]^2$ and $\emptyset_m(t) = \min_{0 < t < t} \emptyset(t) + \eta(t)$. $\eta(t)$ is a white noise added to the minimum position of the potential. The parameters used in the bias potential were: $K = 5 \times 10^5$ eV and the target order parameter $\bar{q}_6^t = 0.6$. The ABMD method was implemented in the PLUMED package⁶².

To corroborate the classical MD results of C₆₀ collapse and polymerization during the early stage of compression, we also conducted ab initio MD simulation to study the phase behaviour of fcc C₆₀ (720 atoms). To this end, the fcc-C₆₀ crystal was first slowly compressed to 30 GPa by geometrical optimization. Then, the phase evolution of the compressed C₆₀ at 30 GPa from 300 to 1,500 K was monitored by conducting ab initio NPT simulation at a heating rate of 2×10^{14} K s⁻¹.

On compression to 30 GPa at 300 K, both classical and ab initio MD simulations demonstrate that the C₆₀ molecules essentially maintain the cage structure but undergo significant deformations (see Extended Data Fig. 6 for details). The compressed C₆₀ molecules are inter-connected by sp³ bonding (the fraction of sp³ bonds is up to ~15% at 30 GPa; Extended Data Fig. 6a). This finding is consistent with our experimental results, where the in situ Raman spectra of C₆₀ indicate the polymerization and deformation of C₆₀ molecules under compression (up to ~32 GPa; Extended Data Fig. 6b). With increasing temperature, temperature-induced sp²–sp³ transition (25% to 70%) mainly occurs between 500 and 1,200 K (Extended Data Figs. 7a and 8). There is a percolation transition of sp³ bonds at 500–800 K, which corresponds to the polymerization of C₆₀ molecules. Hence, from a materials synthesis point of view, a hybrid sp²–sp³ type of amorphous carbon with a controllable fraction of mixed sp²/sp³ bonding can be obtained by heating to different temperatures (most preferably, above 800 K after the percolation transition takes place). On heating to 1,600 K, the proportion of sp³ bonds exceeds 93%. Note that the sp³ fraction was estimated on the basis of the number of four-fold-bonded carbon atoms (that is, CN = 4) within a cutoff distance of 1.85 Å. This value may be slightly underestimated in comparison to that analysed with the maximally localized Wannier function⁹. The structural transition of fcc C₆₀ under 30 GPa is confirmed by ab initio MD simulation (Extended Data Fig. 7b).

Isothermal annealing at high temperatures (for example, 1,600 K) further promotes the sp²–sp³ transition (Extended Data Fig. 7a). The existence of parallel sp³ bonds, due to inter-buckyball connections in the early stage of polymerization (identifiable in Extended Data Fig. 6), persists into the a-D annealed at high temperatures. To illustrate this, we calculate the bond-orientation function of the a-D obtained at 1,600 K, defined as $\Phi(\hat{r}) = \langle \delta\left(\frac{\mathbf{r}_{ij}}{|\mathbf{r}_{ij}|} - \hat{r}\right) \rangle$, where \hat{r} is a unit vector with a random orientation, \mathbf{r}_{ij} refers to an atomic bond between atom i and its nearest neighbour j , and the angular bracket refers to the ensemble average. If all atomic bonds in the system are randomly distributed, one would expect a uniform distribution of $\Phi(\hat{r})$ at all directions. Nonetheless, in compressed C₆₀, despite the seemingly amorphous feature, the sp³ bonds in the a-D have preferred orientations, manifested by the three-dimensional bond-orientation distribution plot and the two-dimensional pole figure (Extended Data Fig. 9). The sp³ bonds with orientational order in a-D provide fertile sites for nucleation and contribute to the nucleation of p-D during isothermal annealing.

Extending the isothermal annealing time up to 15 ns at 1,600 K and 30 GPa, our classical MD simulation reveals the gradual transition

from a-D to p-D via the nucleation and growth mechanism. As shown in Extended Data Fig. 10 and Supplementary Video 1, the fraction of CD- and HD-like paracrystallites gradually increases with prolonged simulation time. Extended Data Fig. 10p and Supplementary Video 1 show the three-dimensional structural model of a p-D with a moderate fraction of paracrystallites (20%) achieved through classical MD. The trajectories of the paracrystallites are illustrated in Extended Data Fig. 10. To further increase the volume fraction of p-D, we resorted to ABMD and the final results are presented in Fig. 3. The appearance of the paracrystallites is dynamically changing, from which one can estimate the critical nucleus size of the paracrystallites (see also Supplementary Video 1).

The critical nuclei are found to contain approximately 20–30 atoms (~3.0 Å), suggesting that the paracrystallites belong to supercritical nuclei. Thermodynamically, these supercritical nuclei have certain probabilities of transitioning back to the amorphous state. Owing to the dynamic fluctuations, the maximum amount of paracrystallites is theoretically limited within a certain fraction (that is, $\phi = 0.7$).

Structural model of NPD. Classical MD was used to generate atomic structures of NPD. To construct the initial structure, the Voronoi tessellation method was used to generate nearly equal-sized nanograins with desirable grain sizes (1.2–2.4 nm). The grains were filled with carbon atoms in diamond cubic arrangements. The as-constructed samples, typically consisting of ~100,000 atoms, were thermally annealed at 1,600 K and 30 GPa for 0.2 ns, followed by relaxations to ambient conditions at 300 K and 0 GPa. The exact grain size of the NPD was computed post-mortem, based on:

$$d = \sqrt[3]{\frac{6N\phi}{\pi n_g}} \quad (4)$$

where N is the total number of atoms, ϕ is the fraction of atoms associated with nanocrystals and n_g is the number of grains.

Structural analysis. For SRO, we proposed a local order parameter s to gauge the similarity between the first two atomic shells of each atom of a-D and that of CD or HD crystal. Inclusion of the second shell in the consideration of the local atomic environment is justified if one is to perform a Voronoi tessellation⁶³ to determine atomic coordination. The similarity order parameter s between cluster A and a reference cluster B is defined as:

$$s^B = \max_{l,\alpha,\beta,\gamma} \frac{N_B \sum_i^{N_A} \sum_j^{N_B} \exp[-|\mathbf{T} \cdot \mathbf{r}_i^A - \mathbf{r}_j^B|^2/\sigma^2]}{N_A \sum_i^{N_B} \sum_j^{N_B} \exp[-|\mathbf{r}_i^B - \mathbf{r}_j^B|^2/\sigma^2]} \quad (5)$$

where N_A and N_B denote the number of atoms in clusters A and B, respectively; \mathbf{r}_i and \mathbf{r}_j are the Cartesian coordinates of the i th and j th atoms in the corresponding cluster; σ is a Gaussian smearing parameter, which is set to 0.15 in this work; \mathbf{T} is a transformation matrix that accounts for affine scaling transformation and cluster rotation, where l is a scaling parameter and α, β and γ are Euler angles for rotation. Having obtained s^{CD} and s^{HD} , we define $s = \max(s^{CD}, s^{HD})$. On the basis of the above definition, s lies between 0 and 1 (for example, two identical clusters would yield $s = 1$ regardless of their respective orientations). A large s value implies a high similarity between the local cluster and the reference crystal (that is, enhanced SRO). The similarity order parameter also provides a facile tool to quantify lattice distortions of the paracrystallites.

For MRO, a local Steinhardt order parameter \bar{q}_6 was used to evaluate the orientational order associated with each atom, which contains ordering information including a few atomic shells. For atom i , the order parameter \bar{q}_6^i was computed by:

$$\bar{q}_6^i = \sum_j^{N_c} \sum_{m=-6}^{m=6} q_{6m}^*(i) q_{6m}(j) \quad (6)$$

where N_c is the total number of atoms included in the coordination shells (that is, MRO clusters, typically up to four atomic shells in this work), and $q_{6m}(i)$ is the Steinhardt vector⁶⁴ of atom i , calculated from:

$$q_{6m}(i) = \sum_k^{\text{CN}} Y_{6m}(r_{ik}) \quad (7)$$

where k loops over all atoms in the nearest neighbours of atom i (in this work, CN = 4), and Y_{6m} is one of the sixth-order spherical harmonics.

While the order parameter \bar{q}_6 yields information about the degree of structural ordering in the system, it is incapable of revealing the exact type of atomic packing (for example, CD versus HD). To mitigate this insufficiency, the CNA method was adopted⁶⁵. The second-nearest neighbours of each atom in CD have fcc packing with a CNA index of 421, whereas for HD, the 12 second-nearest neighbours are arranged in hexagonal close-packing that can be differentiated with a CNA index of 422 (see Extended Data Fig. 5). By performing CNA, each atom can thus be exclusively labelled as the CD-like, HD-like or disordered type.

Having determined the packing type of the atoms, we used the following algorithm to compute the volume fraction of the paracrystallites in the sample ϕ . First, all atoms identified to have CD- or HD-like packing via CNA analysis, together with their 16 nearest neighbours, are considered as paracrystalline atoms. Second, other four-fold-coordinated atoms that are directly bonded to the aforementioned paracrystalline atoms are included in the calculation of ϕ , to account for the ‘boundary’ portion of the paracrystallites. Following this algorithm, we computed the volume fraction of the crystalline component of NPD ($d = 1.56$ nm) to be 94% for benchmarking.

To mathematically quantify the spatial extension of the paracrystallites, we invoked a two-point orientational correlation function, $\kappa(r)$, given by:

$$\kappa(r) = \left\langle \sqrt{\frac{\sum_{m=-6}^{m=6} q_{6m}(i) \cdot q_{6m}^*(j)}{\left| \sum_{m=-6}^{m=6} q_{6m}(i) \right| \cdot \left| \sum_{m=-6}^{m=6} q_{6m}(j) \right|}} \delta(r_{ij} - r) \right\rangle \quad (8)$$

where the bracket indicates that the calculation is averaged over all atomic pairs. The $\kappa(r)$ essentially measures the orientation relationship of two coordination polyhedral at a distance r . In two limiting cases, $\kappa(r) = 1$ for perfect crystals, and $\kappa(r) = 0$ for totally uncorrelated structures. Empirically, we consider $\kappa(r) = 0.3$ as the threshold to estimate the correlation length of the paracrystallites.

Structure factor calculation. Our ab initio modelling provides a reliable and predictive structural model for a-D. Nonetheless, the simulated sample has a finite-size effect. If $S(Q)$ is calculated on the basis of the Fourier transformation of the pair distribution function $g(r)$, truncation ripples will be inevitably incurred in the calculated $S(Q)$. To circumvent this issue, we accurately calculated the structure factors based on the Ornstein–Zernike theory³⁵, which relies on solving for the short-ranged direction correlation function $c(r)$ from the Ornstein–Zernike equation:

$$h(r) = c(r) + \int dr' h(r')c(r') \quad (9)$$

where $h(r) = g(r) - 1$.

In practice, we followed Baxter’s factorization⁶⁶ method together with Dixon–Hutchinson’s numerical algorithm⁶⁷ to obtain $c(r)$ from $g(r)$. Having derived $c(r)$, $S(Q)$ was computed from its Fourier transform $C(Q)$ following:

$$S(Q) = \frac{1}{1 - \rho C(Q)} \quad (10)$$

In this way, we were able to accurately analyse the differences between the structure factors of a-D and p-D without being encumbered by artefacts due to the finite-size effect.

HRTEM simulation

HRTEM image simulations were performed on the basis of a multi-slice algorithm as implemented in MULTEM⁶⁸. The sample thickness was typically 80 Å, and a partial coherence illumination mode was used.

Data availability

The data that support the findings of this study are available from the corresponding authors upon request.

Code availability

The software used for data analysis is available from H.S. upon request.

50. Ishii, T. et al. Generation of pressures over 40 GPa using Kawai-type multi-anvil press with tungsten carbide anvils. *Rev. Sci. Instrum.* **87**, 024501 (2016).
51. Kubo, A. & Akaogi, M. Post-garnet transitions in the system Mg₄Si₄O₁₂–Mg₃Al₂Si₃O₁₂ up to 28 GPa: phase relations of garnet, ilmenite and perovskite. *Phys. Earth Planet. Inter.* **121**, 85–102 (2000).
52. Oliver, W. C. & Pharr, G. M. An improved technique for determining hardness and elastic modulus using load and displacement sensing indentation experiments. *J. Mater. Res.* **7**, 1564–1583 (1992).
53. Kresse, G. & Hafner, J. Ab initio molecular dynamics for liquid metals. *Phys. Rev. B* **47**, 558–561 (1993).
54. Blöchl, P. E. Projector augmented-wave method. *Phys. Rev. B* **50**, 17953–17979 (1994).
55. Wooten, F., Winer, K. & Weaire, D. Computer generation of structural models of amorphous Si and Ge. *Phys. Rev. Lett.* **54**, 1392–1395 (1985).
56. Keating, P. N. Effect of invariance requirements on the elastic strain energy of crystals with application to the diamond structure. *Phys. Rev.* **145**, 637–645 (1966).
57. Mishin, Y., Mehl, M. J. & Papaconstantopoulos, D. A. Phase stability in the Fe–Ni system: investigation by first-principles calculations and atomistic simulations. *Acta Mater.* **53**, 4029–4041 (2005).
58. Brommer, P. & Gähler, F. Potfit: effective potentials from ab initio data. *Model. Simul. Mat. Sci. Eng.* **15**, 295–304 (2007).
59. Cheng, Y. Q., Ma, E. & Sheng, H. W. Atomic level structure in multicomponent bulk metallic glass. *Phys. Rev. Lett.* **102**, 245501 (2009).
60. Laio, A. & Parrinello, M. Escaping free-energy minima. *Proc. Natl Acad. Sci. USA* **99**, 12562–12566 (2002).
61. Maragliano, L. & Vanden-Eijnden, E. A temperature accelerated method for sampling free energy and determining reaction pathways in rare events simulations. *Chem. Phys. Lett.* **426**, 168–175 (2006).
62. Colón-Ramos, D. A., La Rivière, P., Shroff, H. & Oldenbourg, R. Promoting transparency and reproducibility in enhanced molecular simulations. *Nat. Methods* **16**, 670–673 (2019).
63. Finney, J. L. Random packings and the structure of simple liquids. I. The geometry of random close packing. *Proc. R. Soc. Lond. A Math. Phys. Sci.* **319**, 479–493 (1970).
64. Steinhardt, P. J., Nelson, D. R. & Ronchetti, M. Bond-orientational order in liquids and glasses. *Phys. Rev. B* **28**, 784–805 (1983).
65. Stukowski, A. Structure identification methods for atomistic simulations of crystalline materials. *Model. Simul. Mat. Sci. Eng.* **20**, 045021 (2012).
66. Baxter, R. J. Method of solution of the Percus–Yevick, hypernetted-chain, or similar equations. *Phys. Rev.* **154**, 170–174 (1967).
67. Dixon, M. & Hutchinson, P. A method for the extrapolation of pair distribution functions. *Mol. Phys.* **33**, 1663–1670 (1977).
68. Lobato, I., van Aert, S. & Verbeeck, J. Progress and new advances in simulating electron microscopy datasets using MULTEM. *Ultramicroscopy* **168**, 17–27 (2016).
69. Serebryanyaya, N., Blank, V., Ivdenko, V. & Chernozatonskii, L. Pressure-induced superhard phase of C₆₀. *Solid State Commun.* **118**, 183–187 (2001).
70. Kumar, R. S. et al. X-ray Raman scattering studies on C₆₀ fullerenes and multi-walled carbon nanotubes under pressure. *Diam. Relat. Mater.* **16**, 1250–1253 (2007).
71. Solozhenko, V. L., Kurakevych, O. O., Andrault, D., Le Godec, Y. & Mezouar, M. Ultimate metastable solubility of boron in diamond: synthesis of superhard diamondlike BC₅. *Phys. Rev. Lett.* **102**, 015506 (2009).
72. Solozhenko, V. L., Dub, S. N. & Novikov, N. V. Mechanical properties of cubic BC₂N, a new superhard phase. *Diam. Relat. Mater.* **10**, 2228–2231 (2001).
73. Pan, Z., Sun, H., Zhang, Y. & Chen, C. Harder than diamond: superior indentation strength of wurtzite BN and lonsdaleite. *Phys. Rev. Lett.* **102**, 055503 (2009).
74. Blase, X., Gillet, P., Miguel, A. S. & Mélinon, P. Exceptional ideal strength of carbon clathrates. *Phys. Rev. Lett.* **92** (2004).
75. Li, B., Sun, H. & Chen, C. Extreme mechanics of probing the ultimate strength of nanotwinned diamond. *Phys. Rev. Lett.* **117** (2016).
76. Chang, Y. Y., Jacobsen, S. D., Kimura, M., Irfune, T. & Ohno, I. Elastic properties of transparent nano-polycrystalline diamond measured by GHz-ultrasonic interferometry and resonant sphere methods. *Phys. Earth Planet. Inter.* **228**, 47–55 (2014).

Acknowledgements We thank H.K. Mao for insightful discussions. This work was supported by the National Natural Science Foundation of China (grant numbers 12075215 and 61471307), the Fundamental Research Funds for the Central Universities (grant number 20720200075) and the European Research Council under the European Union’s Horizon 2020 research and

Article

innovation programme (proposal no. 787527). The work at George Mason University was supported by the NSF under grant no. DMR-1611064.

Author contributions H.G. and H.S. proposed and supervised the project; H.T., H.F., T.I. and T.K. synthesized the samples; H.T., X.Y., Y.C., F.L. and M.-S.W. performed the structure characterizations; H.T., X.Y., T.L. and Z.Z. measured the properties; H.S. performed the theoretical calculations; H.T., H.S. and H.G. analysed data and wrote the manuscript with the contributions of all authors.

Competing interests The authors declare no competing interests.

Additional information

Supplementary information The online version contains supplementary material available at <https://doi.org/10.1038/s41586-021-04122-w>.

Correspondence and requests for materials should be addressed to Howard Sheng or Huiyang Gou.

Peer review information *Nature* thanks Artem Oganov, Alfonso San Miguel, Yogesh Vohra and the other, anonymous, reviewer(s) for their contribution to the peer review of this work. Peer reviewer reports are available.

Reprints and permissions information is available at <http://www.nature.com/reprints>.